Journal of Alloys and Compounds 509 (2011) 3229–3237

Contents lists available at ScienceDirect

Journal of Alloys and Compounds

journal homepage: www.elsevier.com/locate/jallcom

Heat capacity measurements and XPS studies on uranium–lanthanum mixed oxides

R. Venkata Krishnan [a], V.K. Mittal [b], R. Babu [a], Abhiram Senapati [a], Santanu Bera [b], K. Nagarajan [a,*]

[a] Chemistry Group, Indira Gandhi Centre for Atomic Research, Kalpakkam, India
[b] Water and Steam Chemistry Division, Babha Atomic Research Centre-Facilities, Kalpakkam 603 102, Tamil Nadu, India

ARTICLE INFO

Article history:
Received 6 September 2010
Received in revised form 1 December 2010
Accepted 14 December 2010
Available online 22 December 2010

Keywords:
Uranium
Lanthanum
Mixed oxides
Heat capacity
DSC
Drop calorimetry
Enthalpy increment
Heat capacity anomaly
XPS

ABSTRACT

Heat capacity measurements were carried out on $(U_{1-y}La_y)O_{2\pm x}$ ($y = 0.2$, 0.4, 0.6, and 0.8) using differential scanning calorimeter (DSC) in the temperature range 298–800 K. Enthalpy increment measurements were carried out on the above solid solutions using high temperature drop calorimetry in the temperature range 800–1800 K. Chemical states of U and La in the solid solutions of mixed oxides were determined using X-ray photoelectron spectroscopy (XPS). Oxygen to metal ratios of $(U_{1-y}La_y)O_{2\pm x}$ were estimated from the ratios of different chemical states of U present in the sample. Anomalous increase in the heat capacity is observed for $(U_{1-y}La_y)O_{2\pm x}$ ($y = 0.4$, 0.6 and 0.8) with onset temperatures in the range of 1000–1200 K. The anomalous increase in the heat capacity is attributed to certain thermal excitation process, namely, Frenkel pair defect of oxygen. The heat capacity value of $(U_{1-y}La_y)O_{2\pm x}$ ($y = 0.2$, 0.4, 0.6, and 0.8) at 298 K are 65.3, 64.1, 57.7, 51.9 J K^{-1} mol^{-1}, respectively. From the XPS investigations, it was observed that the O/M ratios at the surface are higher than that in the bulk. In uranium rich mixed oxide samples, the surface O/M ratios are greater than 2 whereas that in La rich mixed oxides, they are less than 2, though the bulk O/M in all the samples are less than 2.

1. Introduction

High temperature heat capacity of the fuel under irradiation is one of the important properties for evaluating the fuel temperature profile during normal operation and the evaluation of fuel temperature under accident conditions. Uranium–plutonium mixed oxides are used as fast reactor fuels. Rare earth fission products (La to Gd) have significant fission yields on fast fission of ^{235}U, ^{238}U and ^{239}Pu [1]. These trivalent rare earth oxides form extensive solid solutions with UO_2 [2]. Hence high temperature heat capacity data of uranium–rare earth mixed oxides are important to predict the fuel behavior during irradiation. Heat capacity of uranium–rare earth mixed oxides has been determined by various authors [3–16]. Anomalous increase in the heat capacity with temperature was reported by various authors [3–11] whereas certain authors [12–16] reported no anomalous increase in the heat capacity. Earlier [11], we have measured the heat capacity of $(U_{1-y}Gd_y)O_{2\pm x}$ ($y = 0.1$, 0.2, and 0.5) by DSC in the temperature range 298–800 K. Considerable anomalous increase in the heat capacity was observed for $(U_{1-y}Gd_y)O_{2\pm x}$ with $y = 0.1$–0.5. To investigate whether similar anomalous increase in the heat capacity with temperature could be observed in case of $(U_{1-y}La_y)O_{2\pm x}$, heat capacity measurements on $(U_{1-y}La_y)O_{2\pm x}$ ($y = 0.2$, 0.4, 0.6, and 0.8) were carried out in this study. These solid solutions were prepared by combustion synthesis and characterized by XRD, HPLC and ICP-AES. The preparation, characterization, solubility studies and thermal expansion measurements by high temperature XRD were reported in our previous publication [17]. In the present investigation, heat capacity of $(U_{1-y}La_y)O_{2\pm x}$ ($y = 0.2$, 0.4, 0.6, and 0.8) were measured by DSC in the temperature range 298–800 K, and their high temperature enthalpy increment measurements in the temperature range 800–1800 K by using drop calorimeter. The chemical states of U and La in their mixed oxide solid solutions have not been studied, previously. In this paper, a detailed analysis of the chemical states of U and La in $(U_{1-y}La_y)O_{2\pm x}$ obtained from XPS is presented. As the depth of the information is limited to few nanometers from the surface of the sample, the oxygen to metal ratio obtained from the XPS results is applicable only to few atomic layers from the surface.

2. Experimental

2.1. Sample preparation and characterization

Sample preparation by combustion synthesis and characterization by XRD, impurity analysis by ICP-MS, etc. of $(U_{1-y}La_y)O_{2\pm x}$ ($y = 0.2$, 0.4, 0.6, and 0.8) have

* Corresponding author at: Fuel Chemistry Division, Chemistry Group, Indira Gandhi Centre for Atomic Research, RCL Building, Kalpakkam 603 102, India. Tel.: +91 44 27480500x24289; fax: +91 44 27480065.
E-mail address: knag@igcar.gov.in (K. Nagarajan).

0925-8388/$ – see front matter © 2010 Elsevier B.V. All rights reserved.
doi:10.1016/j.jallcom.2010.12.090

been discussed in detail in our previous publication [17]. The O/M ratios of the solid solutions were determined by spectrophotometric technique [11] as described below.

The $(U_{1-y}La_y)O_{2\pm x}$ samples were dissolved in concentrated phosphoric acid (2–3 mg/ml). U^{4+} and U^{6+} present in the sample do not change their oxidation states when dissolved in concentrated phosphoric acid whereas U^{5+} is not stable in liquid state and undergoes following disproportionation reaction

$$2U^{5+} \rightarrow U^{4+} + U^{6+} \quad (1)$$

The concentration of U^{4+} was determined by measuring the absorbance at 540 nm and U^{6+} by absorbance at 315 nm [11]. Assuming that the La in the solid solution is present only in +3 valence state and oxygen in −2 valence state, the O/U ratio was determined as follows.

$$\frac{O}{U} = \frac{3n_{U(VI)} + 2n_{U(IV)}}{n_{U(VI)} + n_{U(IV)}} \quad (2)$$

where $n_{U(VI)}$ and $n_{U(IV)}$ are number of moles of U(VI) and U(IV), respectively. The O/M of $(U_{1-y}La_y)O_{2\pm x}$ is calculated as follows:

$$\frac{O}{M} = (1-y)\frac{O}{U} + 1.5y \quad (3)$$

2.2. Calorimetric measurements

A heat flux type differential scanning calorimeter, model number DSC821e/700 of M/s. Mettler Toledo GmbH, Switzerland was used in this study. Temperature, heat and τ-lag calibrations were carried out, as explained in our previous publication [18]. The uncertainty in the heat capacity data measured by DSC was estimated to be in the range of 2–3% based on our previous measurements on standard ThO_2 samples [19]. Prior to each heat capacity measurement heat rate calibration was performed, using a thin disc of sapphire supplied by M/s. Mettler Toledo GmbH. The heat capacity data of sapphire from NIST, USA was used in the calibration. Heat capacity measurements were carried out in the temperature range 298–800 K. To remove any adsorbed moisture on the sample, it was heated to 573 K before starting the experiment. In a typical measurement about 100–150 mg of sample in the form of pellet was weighed accurately and hermetically sealed in a 40 μl Al-pan. The flow rate of the purge gas (ultra high pure argon) was 50 mL min^{-1}. A three segment-heating program, as explained in our previous work [18], was used for heat capacity measurements. Each heat capacity measurement consisted of three runs (1) a blank run with empty pans on the sample and the reference sides, (2) a calibration run with empty pan on the reference side and a pan with sapphire (heat capacity standard) on the sample side and (3) a sample run with empty pan on the reference side and the pan with $(U_{1-y}La_y)O_{2\pm x}$ sample on the sample side.

The enthalpy increments of the samples in the temperature range 800–1800 K were determined by drop calorimetry using a multi-detector high temperature calorimeter (MHTC-96) of M/s. SETARAM. The calorimetric detector is a thermopile which comprises 28 thermocouples embedded on the inner side of an alumina tube. The sample crucible and an empty reference crucible are positioned one above the other in the calorimetric detector. The thermocouples of the thermopile detector are positioned at different levels surrounding the outer surfaces of the crucibles so that an integrated heat exchange between the two crucibles is obtained as the output signal. In the present study, a detector, made of Pt-30%Rh/Pt-10% thermocouples was employed. The detector is centered in a leak-tight alumina muffle placed in a graphite resistance furnace.

In a typical experiment, five samples of α-alumina reference (SRM 720) material and five samples of $(U_{1-y}La_y)O_{2\pm x}$, each weighing about 150–200 mg, were initially placed in the individual slots of the specimen chamber kept at ambient temperature. The α-alumina references and $(U_{1-y}La_y)O_{2\pm x}$ samples were placed in such a way that each $(U_{1-y}La_y)O_{2\pm x}$ sample was sandwiched between two α-alumina references. The furnace was gradually heated to the desired preset temperature and argon was passed through the furnace. Once the temperature of the furnace reached the measurement temperature, the samples were dropped from the specimen chamber. The samples maintained at the ambient temperature fell into the sample crucible maintained at temperature (T). About 20–25 min was found to be sufficient for the re-stabilization of both the temperature and the heat flow signals. The heat flow, Q (in μV) was monitored as a function of time (t) and the peak area $\int Q\,dt$ (after subtracting the baseline) associated with each drop corresponded to the respective enthalpy increment. From the resultant heat flow signals corresponding to the α-alumina reference (Q_R) and the sample (Q_S), the enthalpy increments $(H_T - H_{298})_S$ of samples were computed using the known enthalpy increment values of α-alumina reference $(H_T - H_{298})_R$ from the literature [20] and the following expression

$$(H_T - H_{298})_S = \frac{\int Q_S\,dt}{\int Q_R\,dt}\frac{M_S}{m_S}\frac{m_R}{m_R}(H_T - H_{298})_R \quad (4)$$

where M_R and m_R are the molar mass and mass of the α-alumina reference pellet and M_S and m_S are the molar mass and mass of the mixed oxide sample. The mean of the five heat flow values for the standard and that for the sample were used to compute the enthalpy increment at that temperature, T. Further, four or five measurements were carried out for a given temperature and the mean value of the enthalpy increments from these runs at temperature, T were used for fitting.

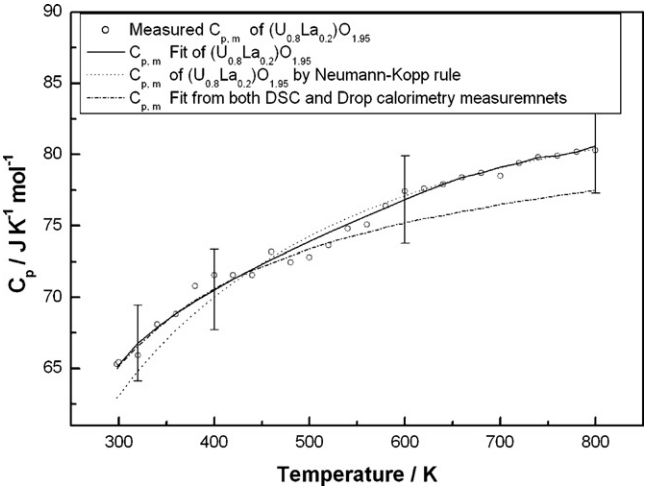

Fig. 1. Heat capacity data of $(U_{0.8}La_{0.2})O_{1.95}$ measured by DSC.

2.3. XPS studies

XPS studies were carried out using VG ESCALAB MKII system. The base vacuum of the chamber was 10^{-10} mbar and AlKα was used as excitation source for photoelectron emission.

3. Results

3.1. Heat capacity measurements by DSC

Heat capacity of $(U_{1-y}La_y)O_{2\pm x}$ (y = 0.2, 0.4, 0.6, and 0.8) measured by DSC are the mean of nine measurements. The measured heat capacity values of samples were least square fitted to a polynomial in temperature. The measured heat capacity data of the mixed oxides along with the fit values are shown in Figs. 1–4 and are also listed in Tables 1–4. The heat capacity data estimated by Neumann–Kopp's law using the literature heat capacity data of La_2O_3 [21] and UO_2 [22] are also given in Figs. 1–4. The corrections for non-stoichiometry in the heat capacity values were made using the method described by Mills et al. [7].

$$C_{p,m}(UO_2) = \frac{3}{3+x}C_{p,m}(UO_{2+x}) \quad (5)$$

In our previous publication [11] on the heat capacity of $(U_{1-y}Gd_y)O_{2\pm x}$ (y = 0.1, 0.2 and 0.5) considerable anomalous increase in the heat capacity was observed in the temperature range

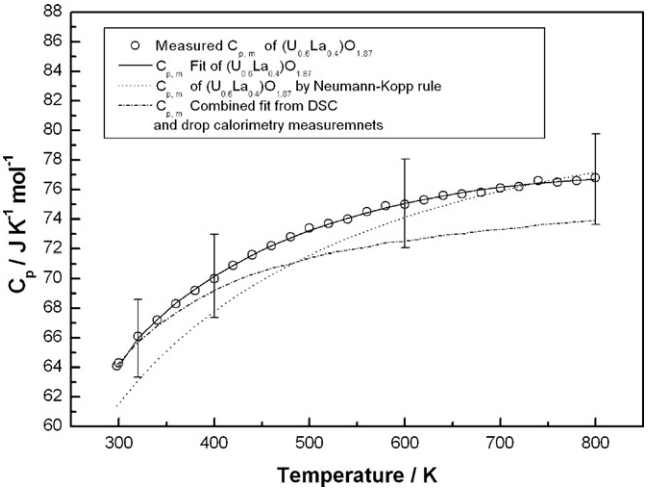

Fig. 2. Heat capacity data of $(U_{0.6}La_{0.4})O_{1.87}$ measured by DSC.

Table 1
Thermodynamic functions for $(U_{0.8}La_{0.2})O_{1.95}$.

T (K)	$C_{p,m}$ (J K^{-1} mol^{-1})		$H_T - H_{298}$ (J mol^{-1})		S_T (J K^{-1} mol^{-1})	$G_T - H_{298}/T$ (J K^{-1} mol^{-1})
	Measured	Fit	Measured	Fit		
298	65.3	65.0		0	87.6	−87.6
300	65.5	65.2		130	88.0	−87.6
400	71.6	70.6		6943	107.6	−90.2
500	72.8	73.4		14,146	123.7	−95.4
600	77.4	75.2		21,572	137.2	−101.2
700	78.5	76.5		29,148	148.9	−107.2
800	80.3	77.5	36,999	36,837	159.1	−113.1
900		78.3	44,796	44,618	168.3	−118.7
1000		79.0	52,666	52,477	176.6	−124.1
1100		79.7	60,598	60,405	184.1	−129.2
1200		80.3	68,589	68,394	191.1	−134.1
1300		80.8	76,634	76,439	197.5	−138.7
1400		81.3	84,731	84,536	203.5	−143.1
1500		81.8	92,877	92,681	209.1	−147.4
1600		82.2	101,071	100,872	214.4	−151.4
1700		82.6	109,313	109,104	219.4	−155.2
1800		83.0	117,600	117,375	224.2	−158.9

Table 2
Thermodynamic functions for $(U_{0.6}La_{0.4})O_{1.87}$.

T (K)	$C_{p,m}$ (J K^{-1} mol^{-1})		$H_T - H_{238}$ (J mol^{-1})		S_T (J K^{-1} mol^{-1})	$G_T - H_{298}/T$ (J K^{-1} mol^{-1})
	Measured	Fit	Measured	Fit		
298	64.1	64.2		0	79.1	−79.1
300	64.3	64.3		129	79.6	−79.1
400	70.0	69.2		6840	98.8	−81.7
500	73.4	71.4		13,880	114.5	−86.8
600	75.0	72.5		21,080	127.7	−92.5
700	76.1	73.3		28,373	138.9	−98.4
800	76.8	73.9	34,910	35,733	148.7	−104.1
900		74.4	42,252	43,148	157.5	−109.5
1000		75.0	49,690	50,619	165.4	−114.7
1100		75.6	57,219	58,147	172.5	−119.7
1200		76.3	64,838	65,739	179.1	−124.4
1300		77.0	72,544	73,402	185.3	−128.8
1400		77.9	80,336	81,146	191.0	−133.1
1500		78.8	88,214	88,978	196.4	−137.1
1600		79.9	96,177	96,910	201.5	−141.0
1700		81.0	104,224	104,952	206.4	−144.7
1800		82.3	112,354	113,114	211.1	−148.2

500–600 K. This phenomenon was attributed to the formation of Frenkel-pair like defects of oxygen [4–6,8–10]. This is because the formation of large number of Frenkel-pair defects of oxygen is enabled, when UO_2 is doped with aliovalent cations (La^{3+} in this case). Arita et al. [8] suggested that doping of trivalent cations in UO_2 produces greater complexity of oxygen arrangements, which in turn, induces the formation of oxygen defects resulting in the heat capacity anomaly. However, in the present heat capacity measurements on $(U_{1-y}La_y)O_{2\pm x}$ (y = 0.2, 0.4, 0.6, and 0.8) by DSC in the temperature range 298–800 K no such anomalous increase in

Table 3
Thermodynamic functions for $(U_{0.4}La_{0.6})O_{1.87}$.

T (K)	$C_{p,m}$ (J K^{-1} mol^{-1})		$H_T - H_{298}$ (J mol^{-1})		S_T (J K^{-1} mol^{-1})	$G_T - H_{298}/T$ (J K^{-1} mol^{-1})
	Measured	Fit	Measured	Fit		
298	57.7	57.5		0	72.1	−72.1
300	57.8	57.7		116	72.5	−72.1
400	64.6	64.5		6280	90.2	−74.5
500	68.3	67.4		12,896	105.0	−79.2
600	69.2	69.0		19,725	117.4	−84.5
700	71.8	69.8		26,670	128.1	−90.0
800	74.3	70.5	32,834	33,688	137.5	−95.4
900		70.9	39,822	40,762	145.8	−100.5
1000		71.4	46,899	47,883	153.3	−105.4
1100		71.9	54,058	55,053	160.1	−110.1
1200		72.5	61,296	62,274	166.4	−114.5
1300		73.1	68,608	69,554	172.3	−118.7
1400		73.8	75,993	76,900	177.7	−122.8
1500		74.6	83,450	84,319	182.8	−126.6
1600		75.4	90,976	91,823	187.7	−130.3
1700		76.4	98,571	99,420	192.3	−133.8
1800		77.5	106,235	107,120	196.7	−137.2

Table 4
Thermodynamic functions for $(U_{0.2}La_{0.8})O_{1.71}$.

T (K)	$C_{p,m}$ (J K^{-1} mol^{-1})		$H_T - H_{298}$ (J mol^{-1})		S_T (J K^{-1} mol^{-1})	$G_T - H_{298}/T$ (J K^{-1} mol^{-1})
	Measured	Fit	Measured	Fit		
298	51.9	51.6		0	66.5	−66.5
300	51.9	51.8		104	66.9	−66.5
400	58.0	58.7		5678	82.9	−68.7
500	62.2	61.8		11,721	96.3	−72.9
600	65.4	63.6		18,000	107.8	−77.8
700	68.9	64.8		24,423	117.7	−82.8
800	69.5	65.7	30,232	30,948	126.4	−87.7
900		66.4	36,762	37,555	134.2	−92.4
1000		67.2	43,405	44,238	141.2	−97.0
1100		67.9	50,154	50,996	147.7	−101.3
1200		68.7	57,004	57,833	153.6	−105.4
1300		69.6	63,954	64,753	159.1	−109.3
1400		70.5	71,000	71,764	164.3	−113.1
1500		71.6	78,141	78,872	169.2	−116.7
1600		72.7	85,376	86,087	173.9	−120.1
1700		73.9	92,705	93,418	178.3	−123.4
1800		75.1	100,125	100,872	182.6	−126.6

the heat capacity was observed. To study whether such anomalies could be observed at higher temperatures, enthalpy increment measurements were carried out on these samples from 800 K to 1800 K.

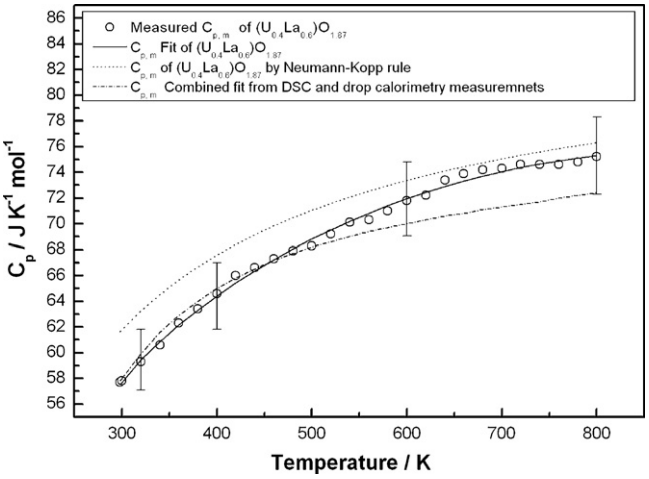

Fig. 3. Heat capacity data of $(U_{0.4}La_{0.6})O_{1.87}$ measured by DSC.

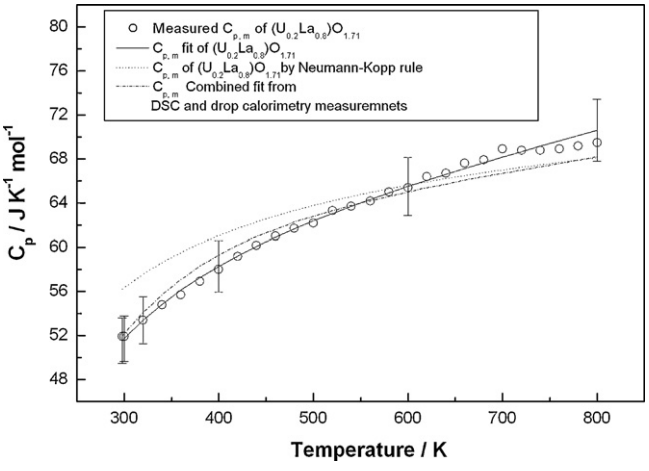

Fig. 4. Heat capacity data of $(U_{0.2}La_{0.8})O_{1.71}$ measured by DSC.

3.2. Enthalpy increment measurements by drop calorimetry

The accuracy of the enthalpy increments from drop calorimetric measurements had been determined to be 2–4% from the heat capacity measurements on standard ThO_2 samples [23]. The measured enthalpy increments of $(U_{1-y}La_y)O_{2\pm x}$ (y = 0.2, 0.4, 0.6, 0.8) in the temperature range of 800–1800 K are the mean of five measurements. They are given in Tables 1–4, respectively. The standard deviation of the enthalpy increment is in the range of 2–4%. The enthalpy increment data were fitted to the following polynomial function in temperature by the method of least squares, using the following two constraints: (i) $H_T - H_{298} = 0$ at 298 K; (ii) the derivative of the function at 298 K is equal to the value of heat capacity at 298 K obtained by DSC.

$$H_T - H_{298} \quad (\text{J mol}^{-1}) = A\frac{T}{K} + B \times 10^{-3}\left(\frac{T}{K}\right)^2 + C \times 10^5 \frac{K}{T} + D \times 10^4 \qquad (6)$$

The measured enthalpy increment data of $(U_{1-y}La_y)O_{2\pm x}$ (y = 0.2, 0.4, 0.6, and 0.8) along with the fit values are shown in Fig. 5 and are also listed in Tables 1–4. The fit parameters of the enthalpy incre-

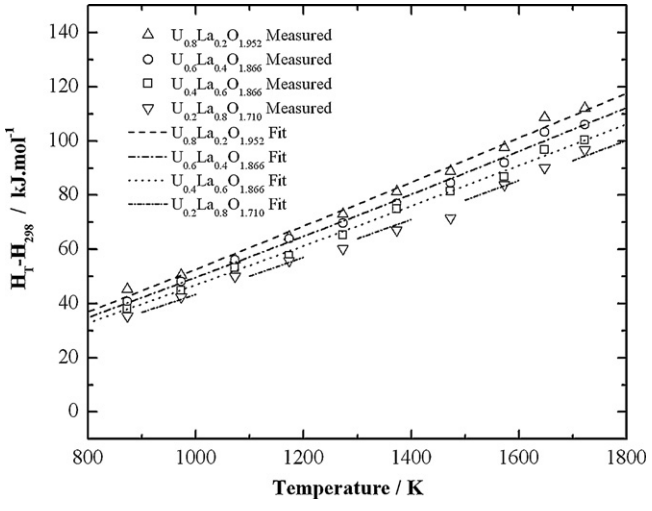

Fig. 5. Enthalpy increment data of $(U_{1-y}La_y)O_{2\pm x}$ by drop calorimetry.

Table 5
Coefficients of the fit equations of the measured enthalpy data ($800 \leq T/K \leq 1800$).

Coefficients	$(U_{0.8}La_{0.2})O_{1.95}$	$(U_{0.6}La_{0.4})O_{1.87}$	$(U_{0.4}La_{0.6})O_{1.87}$	$(U_{0.2}La_{0.8})O_{1.71}$
A	75.9035	67.1605	65.6287	58.9321
B	2.0922	4.0880	3.2278	4.4434
C	10.6771	4.9764	8.9368	8.5175
D	−2.6397	−2.2056	−2.2851	−2.0822
Standard error ($J\,mol^{-1}$)	2661	1577	1508	2215

Table 6
Fitting equations of the measured heat capacity data obtained from DSC and drop calorimetry ($298 \leq T/K \leq 1800$).

S. No	Compound	Fit equation ($J\,K^{-1}\,mol^{-1}$)	Standard error ($J\,K^{-1}\,mol^{-1}$)
1	$(U_{0.8}La_{0.2})O_{1.95}$	$74.21276 + 0.00676\,(T/K) - 989{,}343.42078\,(K/T)^2 - 9.5364 \times 10^{-7}\,(T/K)^2$	0.24
2	$(U_{0.6}La_{0.4})O_{1.87}$	$78.17408 - 0.00778\,(T/K) - 1{,}084{,}417.13{,}722\,(K/T)^2 + 5.6957 \times 10^{-6}\,(T/K)^2$	0.71
3	$(U_{0.4}La_{0.6})O_{1.87}$	$76.8715 - 0.00963\,(T/K) - 1{,}508{,}439.04313\,(K/T)^2 + 5.6886 \times 10^{-6}\,(T/K)^2$	0.88
4	$(U_{0.2}La_{0.8})O_{1.71}$	$69.27049 - 0.00583\,(T/K) - 1{,}457{,}155.61469\,(K/T)^2 + 5.1915 \times 10^{-6}\,(T/K)^2$	0.78

ment data (Eq. (3)) along with the standard errors of the fit are given in Table 5. From the above fit equations the heat capacity data in the temperature range 800–1800 K were computed. Further, this heat capacity data were combined with the heat capacity data from DSC at low temperatures (298–800 K). The combined fit of the measured heat capacity data of $(U_{1-y}La_y)O_{2\pm x}$ ($y = 0.2$, 0.4, 0.6, and 0.8) by DSC in the temperature range 298–800 K and that computed from the enthalpy increment measurements by drop calorimeter in the temperature range 800–1800 K are shown in Tables 1–4. The equations for the combined fit (DSC and drop calorimetric measurements) on the heat capacity of $(U_{1-y}La_y)O_{2\pm x}$ ($y = 0.2$, 0.4, 0.6, and 0.8) in the temperature range 298–1800 K are given in Table 6. As can be seen in Tables 1–4 and Figs. 1–4, the combined fit is lower than the measured data by 1–3% in the temperature range 298–600 K and therefore within the experimental uncertainty of 2–3% [19]. However, it is much lower (3–5%) in the temperature range 700–800 K. In our opinion we recommend the data computed from the combined fit rather than the data from the measurement using single technique.

From the heat capacity data other thermodynamic functions such as enthalpy, entropy and Gibbs energy functions were computed and are given in Tables 1–4. The S_{298} data of $(U_{1-y}La_y)O_{2\pm x}$, required for the computation of entropies were estimated by Neumann–Kopp's law using the literature data of S^0_{298} of pure La_2O_3 [21] and UO_2 [22] besides including the contribution of entropy of mixing.

3.3. XPS studies

3.3.1. U 4f photoelectron peak analysis

Uranium $4f_{7/2}$ peaks from $(U_{1-y}La_y)O_{2\pm x}$ samples were taken for the analysis. The binding energy difference between U^{4+} and U^{6+} states is around 1.2 eV [24,25]. The marginal difference in the binding energy of different chemical states of U lead to the convolution of peaks and therefore resulting in a higher full width at half maximum (FWHM) than the individual peak widths.

In case of $(U_{0.4}La_{0.6})O_{2\pm x}$, the peak at peak position of 380.7 eV fits perfectly with a peak width of 2.0 eV (Fig. 6b). This along with a distinct satellite peak in the range of 7.8–8.2 eV (from the principle peak position) [24] and the absence of other satellite peaks corresponding to U^{4+} and U^{6+} proves that only U^{5+} is present in this sample. Hence the peak width of 2.0 eV is taken as standard for fitting U^{5+} in the other oxides. In Fig. 6a, the satellite peak of U 4f peak obtained from $(U_{0.8}La_{0.2})O_{2\pm x}$ is seen to be different from that observed in $(U_{0.4}La_{0.6})O_{2\pm x}$. The satellite peak in $(U_{0.8}La_{0.2})O_{2\pm x}$ was observed to have characteristic satellite peaks from both U^{5+} and U^{4+}. Based on the satellite peak position, peak width and peak asymmetry, the peaks were deconvoluted into different U valency states as shown in Fig. 7. The measured peak widths of U $4f_{7/2}$ of $(U_{0.8}La_{0.2})O_{2\pm x}$ and $(U_{0.6}La_{0.4})O_{2\pm x}$ oxides (Table 7) are higher than that of U^{4+} (2.2 eV) [24,25]. Therefore, the composite peaks of the these samples were resolved by fitting the Gaussian–Lorentzian line-shape functions using the peak positions and FWHM values for the respective oxidation states taken from similar standard compounds. The deconvoluted peaks which corresponding to various chemical states of U as shown in Fig. 7. Table 7 shows the deconvolution parameters of different chemical states of U in $(U_{0.8}La_{0.2})O_{2\pm x}$ and $(U_{0.6}La_{0.4})O_{2\pm x}$. In the case of $(U_{0.2}La_{0.8})O_{2\pm x}$, the satellite peak position at 7.8 eV indicates the presence of U^{5+} state in the oxide. But higher peak width and asymmetric peak shape at the higher energy side of the peak indicates the presence of U^{6+} state also. The composite peaks are resolved as mentioned earlier and the deconvoluted peaks corresponding to U^{5+} and U^{6+} are shown in Fig. 7. Fig. 6 shows a typical U 4f photoelectron peaks obtained of $(U_{0.8}La_{0.2})O_{2\pm x}$ and $(U_{0.4}La_{0.6})O_{2\pm x}$ and the mark on the spectrum shows the presence of distinct satellite characteristic of U^{5+} and U^{4+}. The concentration of different chemical states of U present in the oxides is given in Table 7.

3.3.2. La 3d photoelectron peak analysis

Lanthanum compounds show multi component structures in 3d core level spectra as shown in Fig. 8. Oxidation state of La

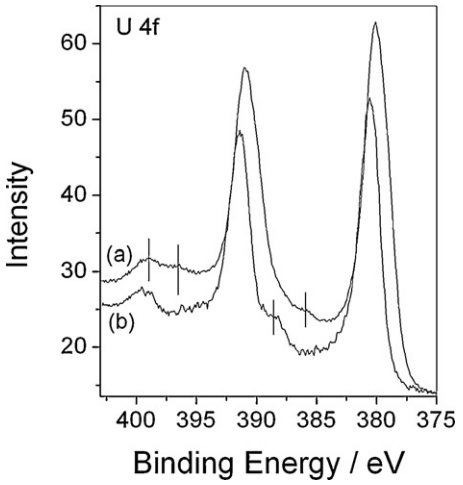

Fig. 6. Typical U 4f photoelectron peaks obtained from (a) $(U_{0.8}La_{0.2})O_{2\pm x}$ and (b) $(U_{0.4}La_{0.6})O_{2\pm x}$. The mark on the spectrum shows the presence of distinct satellite characteristic of U^{5+} and U^{4+}.

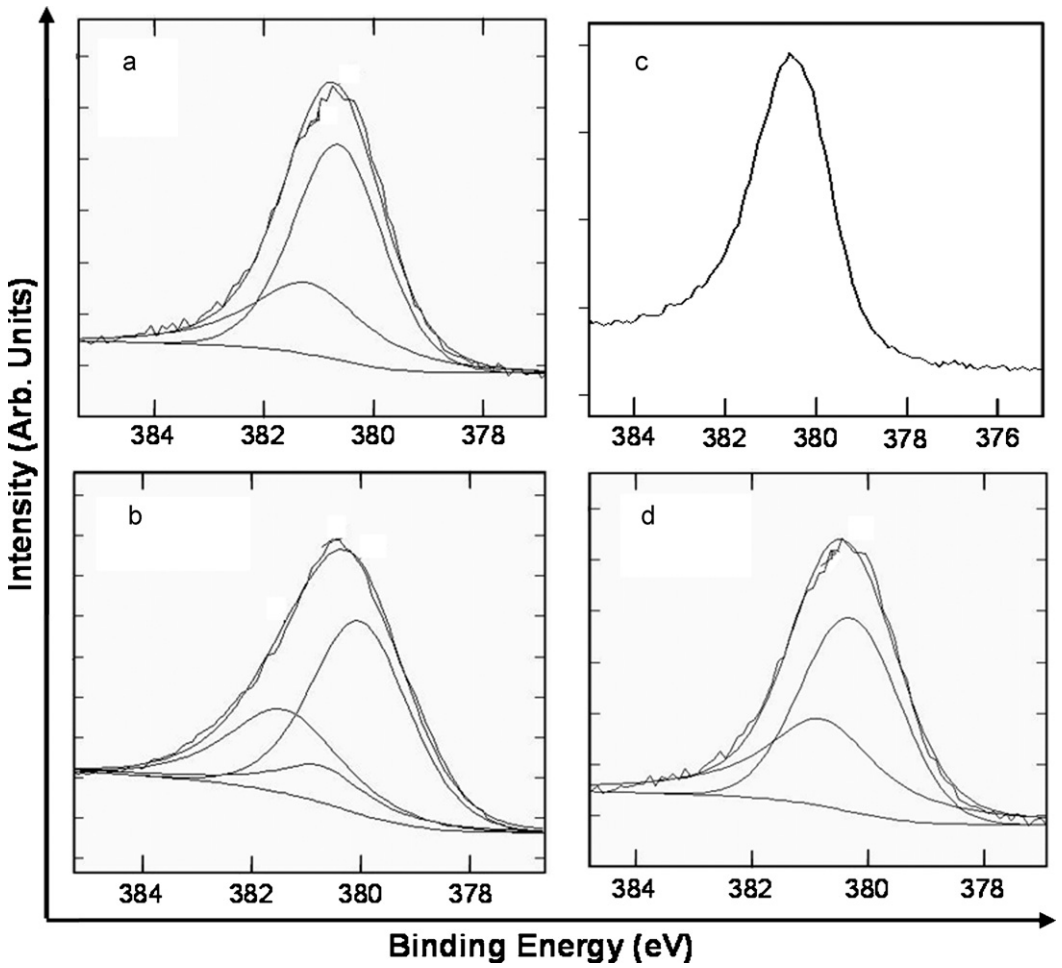

Fig. 7. Deconvolution of U $4f_{7/2}$ photoelectron peaks obtained from (a) $(U_{0.8}La_{0.2})O_{2\pm x}$, (b) $(U_{0.6}La_{0.4})O_{2\pm x}$, (c) $(U_{0.4}La_{0.6})O_{2\pm x}$ and (d) $(U_{0.2}La_{0.8})O_{2\pm x}$.

is +3 in all the oxides, though the peak shapes vary. The difference in the peak shape are due to the fact that La-oxide is hygroscopic in nature resulting to partial formation of surface La-hydroxide which has higher binding energy compared to La-oxide [27]. The signature of hydroxide formation was also found in O 1s peak.

3.3.3. O 1s photoelectron peak analysis

Oxygen 1s spectra shown in Fig. 9 confirmed the formation of hydroxide at the surface of the oxide in [27]. The higher energy peak around 531 eV corresponds to the hydroxide peak and the other peak corresponds to oxygen in the lattice of $(U_{1-y}La_y)O_{2\pm x}$. From Fig. 9, it has been observed that the amount of hydroxide formation on the surface increased with increase in La content in the sample. It is attributed to the inherent hygroscopic nature of lanthanum oxide as explained above.

3.3.4. O/U and O/M calculation

As can be seen from Table 7, $(U_{1-y}La_y)O_{2\pm x}$ contains multiple oxidation states of U. Uranium in lanthanum rich mixed oxide is present only in U^{5+} and U^{6+} states whereas in U rich mixed oxide, it is present predominantly as U^{4+} and U^{5+} states. La was found to be present in only La^{3+} state. The amounts of different chemical states of U are given in Table 7. Oxygen to metal ratio (O/M) could not be estimated accurately from the peak area under O 1s and the peak area of U and La photoelectrons. This is because, the surface is generally contaminated with adsorbed oxygen and therefore calculation of O content from the spectra would lead to over estimation of oxygen. However, the amount of oxygen on the surface depends on the chemical states of the metals below the oxygen layer [26,28]. La is present only in +3 states, while U is present in +4, +5 and +6 states. The O/M in the samples was estimated from the composition of chemical states of the metal ions present in the escape depth

Table 7
Different peak parameters of U $4f_{7/2}$ before and after deconvolution showing the presence of different oxidation states of uranium.

Sample	Peak centre (FWHM) (eV)	Satellite peak (eV)	Deconvoluted peak centre (eV)	FWHM (eV)	Oxidation state	Relative atomic conc. (%)
$(U_{0.8}La_{0.2})O_{2\pm x}$	380.3 (2.5)	8.2	380.7	2.0	+5	37
		5.5	379.9	2.2	+4	63
$(U_{0.6}La_{0.4})O_{2\pm x}$	380.6 (2.7)	8.2	381.3	2.3	+6	30
			380.6	2.0	+5	11
			379.9	2.2	+4	59
$(U_{0.4}La_{0.6})O_{2\pm x}$	380.7 (2.0)	7.8	380.7	2.0	+5	100
$(U_{0.2}La_{0.8})O_{2\pm x}$	380.4 (2.3)	7.8	380.8	2.3	+6	33
			380.3	2.0	+5	67

Table 8
Comparison of O/M and O/U ratio obtained from spectrophotometric and XPS techniques.

Sample	O/U spectrophotometric	O/U XPS	O/M spectrophotometric	O/M XPS
$(U_{0.8}La_{0.2})O_{2\pm x}$	2.065	2.185	1.952	2.048
$(U_{0.6}La_{0.4})O_{2\pm x}$	2.110	2.355	1.866	2.013
$(U_{0.4}La_{0.6})O_{2\pm x}$	2.414	2.500	1.866	1.900
$(U_{0.2}La_{0.8})O_{2\pm x}$	2.552	2.665	1.710	1.733

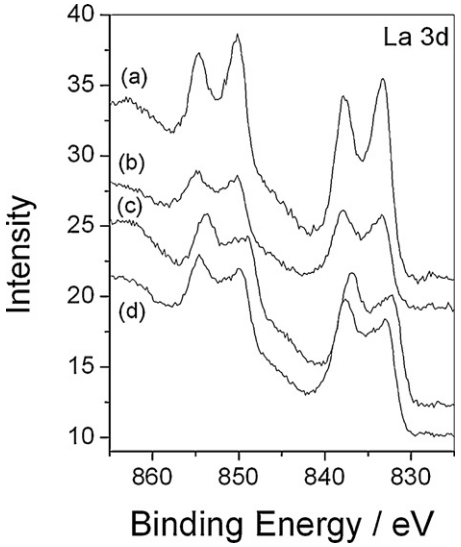

Fig. 8. La 3d photoelectron spectra obtained from (a) $(U_{0.8}La_{0.2})O_{2\pm x}$, (b) $(U_{0.6}La_{0.4})O_{2\pm x}$, (c) $(U_{0.4}La_{0.6})O_{2\pm x}$ and (d) $(U_{0.2}La_{0.8})O_{2\pm x}$.

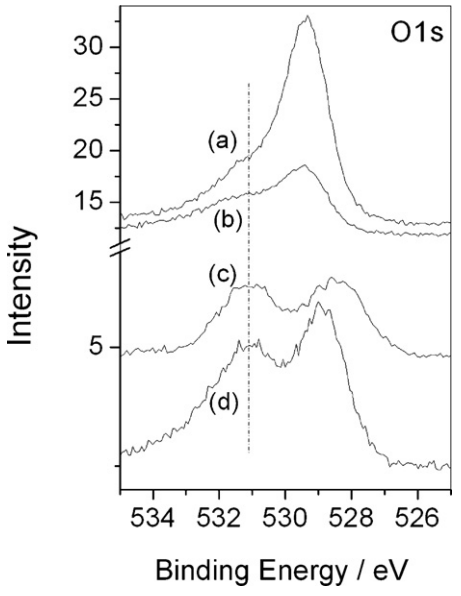

Fig. 9. O 1s photoelectron peaks obtained from different oxides (a) $(U_{0.8}La_{0.2})O_{2\pm x}$, (b) $(U_{0.6}La_{0.4})O_{2\pm x}$, (c) $(U_{0.2}La_{0.8})O_{2\pm x}$ and (d) $(U_{0.4}La_{0.6})O_{2\pm x}$.

region of the sample assuming charge neutrality. The O/M and O/U computed from the amounts of different chemical states of metal ions present in the sample are given in Table 8.

4. Discussion

The combined fit of the heat capacity data obtained from the DSC and drop calorimetric experiments is shown in Fig. 10. As seen in Fig. 10, considerable anomalous increase in the heat capacity is observed with onset temperatures in the range 1000–1200 K for $(U_{1-y}La_y)O_{2\pm x}$ ($y = 0.4$, 0.6, and 0.8) whereas for $y = 0.2$ no such anomaly was observed in the entire temperature range of measurement. The onset temperature of anomalous increase in the heat capacity did not vary with lanthanum content in the sample. The present observed heat capacity anomaly might also be due to predominant contribution of formation of Frenkel pairs of oxygen defects, as it was observed in our previous study on heat capacity of $(U_{1-y}Gd_y)O_{2\pm x}$ [11]. This is because the formation of large number of Frenkel-pair defects of oxygen is enabled when UO_2 is doped with aliovalent cations (La^{3+} in this case) [4–11]. The baseline heat capacity of $(U_{1-y}\ La_y)O_{2\pm x}$ ($y = 0.2$, 0.4, 0.6, and 0.8) was obtained from a least squares fitting for the data in the temperature region 298–1200 K and extrapolating up to 1800 K. The baseline and combined heat capacity data were fitted using the following equations, respectively

$$C_p = A + BT + CT^{-2} \quad (7)$$

$$C_p = A + BT + CT^{-2} + DT^2 \quad (8)$$

The difference between the baseline heat capacity and that of the measured heat capacity data gives the excess heat capacity (ΔC_p) [5]. The excess heat capacity is plotted against temperature for all the solid solutions in Fig. 11. As can be seen in Fig. 11, the onset temperature of heat capacity anomaly is in the region of 1000–1200 K. In our previous study [11] on the heat capacity of $(U_{1-y}Gd_y)O_{2\pm x}$ by DSC, it was observed that the onset temperature of anomaly is in the region of 500–600 K and decreases with increase in gadolinium content. However, in the heat capacity of $(U_{1-y}La_y)O_{2\pm x}$ the onset temperature of heat capacity anomaly did not vary with lanthanum content in the sample and is observed only for $y \geq 0.4$. This may be due to difference in the enthalpies of defect formation between the two mixed oxides. To examine the above reason the enthalpy of the defect formation was computed from the following relation.

If E_d is the energy needed to form a defect, the number of defects, n_d at any temperature T will be given by

$$n_d = n_0 \exp(-E_d/kT) \quad (9)$$

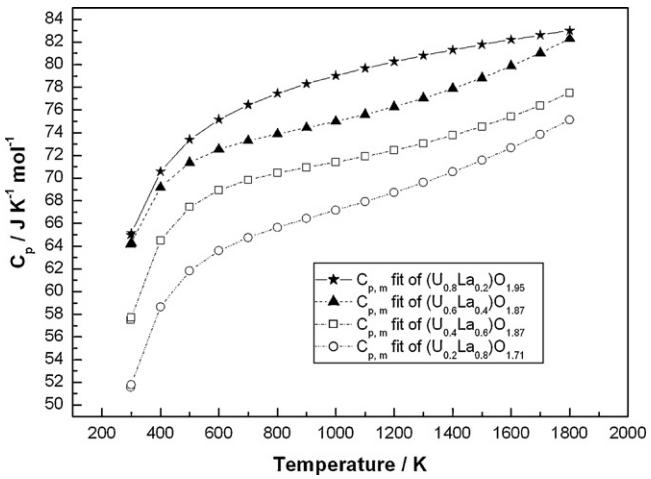

Fig. 10. Combined fit of the heat capacity of $(U_{1-y}La_y)O_{2\pm x}$ from DSC and drop calorimetric measurements.

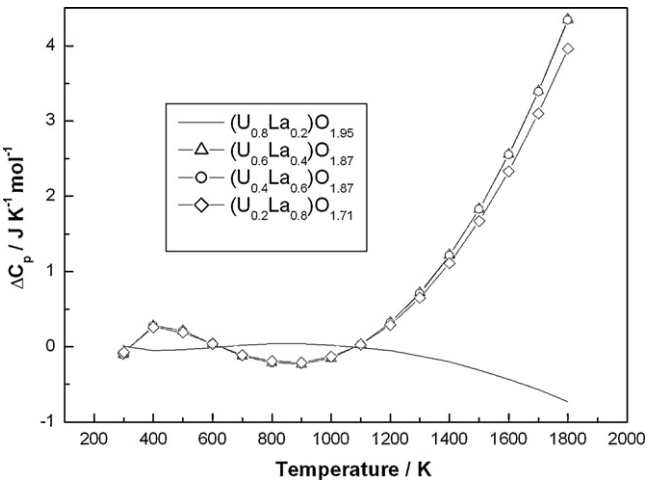

Fig. 11. Difference between the baseline and measured heat capacity data (ΔC_p) vs T of $(U_{1-y}La_y)O_{2\pm x}$.

and the specific heat of formation of such defects will be given by

$$\Delta C_v = \frac{d}{dT}(n_d E_d) = \frac{n_0 E_d^2}{kT^2 \exp(-E_d/kT)} \quad (10)$$

Thus, a plot of $\ln(T^2 \Delta C_v)$ against $1/T$ will be a straight line with a slope of $-E_d/k$. Similarly, a plot of $\ln(T^2 \Delta C_p)$ against $1/T$ is a straight line with a slope of $-\Delta H_d/k$, where ΔH_d is the enthalpy of formation of the defect. The plot of $\ln(T^2 \Delta C_p)$ against $1/T$ for $(U_{1-y}La_y)O_{2\pm x}$ ($y = 0.4$, 0.6, and 0.8) is shown in Fig. 12 and the enthalpy of defect formation computed from the slopes are 1.31, 1.33 and 1.31 eV, respectively. The enthalpy of defect formation computed from our previous study [11] on $(U_{1-y}Gd_y)O_{2\pm x}$ is in the range of 0.57–0.81 eV depending on the concentration of Gd. It has also been observed [11] that the enthalpy of defect formation decreases with increase in the concentration of Gd in the mixed oxide sample and reaches a plateau for $y \geq 0.15$. The present data for enthalpy of defect formation of $(U_{1-y}La_y)O_{2\pm x}$ suggests that the plateau region for this mixed oxide may be in the range $0.2 \leq y \leq 0.4$. The absence of anomalous increase in the heat capacity is in the case of $y = 0.2$ may be due to the higher enthalpy of the defect formation, in the case of La doped UO_2 compared to Gd doped UO_2 and therefore could be observed only at higher temperatures. Matsui et al. [5] observed anomalous increase in the heat capacity in $(U_{1-y}La_y)O_{2\pm x}$ in compositions $y < 0.2$ and computed the enthalpy

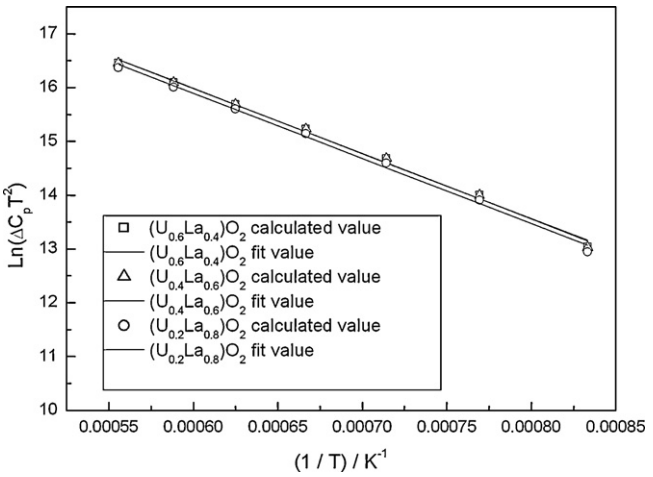

Fig. 12. Plot of $\ln(T^2 \Delta C_p)$ vs $1/T$ in the temperature range 1200–1800 K.

of defect formation in the range of 1.5–2.14 eV. However, in the present measurement the heat capacity anomaly is observed only for $y \geq 0.4$. This may be due to the difference between the oxygen stoichiometry of the present sample from that of Matsui et al. [5].

The enthalpy of defect formation computed for $(U_{1-y}Gd_y)O_{2\pm x}$ [11] is in the range of 0.57–0.81 eV and from the present study that of $(U_{1-y}La_y)O_{2\pm x}$ computed is in the range of 1.31–1.33 eV. The difference in enthalpy of the defect formation could be explained in terms of difference in elastic strain experienced by the fluorite lattice of UO_2 due to doping of trivalent lanthanide. The elastic strain $|\Delta a|$ is the lattice parameter change per mol% of trivalent dopant doped in UO_2. The $|\Delta a|$ from the experimental lattice parameter of $(U_{1-y}Gd_y)O_{2\pm x}$ is in the range of 0.005–0.007 nm whereas that of $(U_{1-y}La_y)O_{2\pm x}$ is in the range 0.118–0.126 nm.

Explanations are available in the literature [29–31] on the differences in the ionic conductivities of the trivalent doped MO_2 fluorite solid-solutions, on the basis of the differences in the elastic strain. The ionic conductivity of the trivalent doped fluorite type oxides, such as UO_2, CeO_2, and ThO_2 where oxygen is the predominant mobile species is higher for solid solutions experiencing lower elastic strain $|\Delta a|$ on doping. The Frenkel defect pair of oxygen is formed more easily under the condition that makes oxygen ions more mobile [6] which in turn could be achieved by doping UO_2 resulting in low elastic strain $|\Delta a|$. In other words, the enthalpy of defect formation increases with increase in $|\Delta a|$ suggesting that the larger elastic strain suppresses the formation of Frenkel pair like defect of oxygen and thus, increases the enthalpy of defect formation. The enthalpy of defect formation and the higher onset temperature of the heat capacity anomaly for $(U_{1-y}La_y)O_{2\pm x}$ compared to that of $(U_{1-y}Gd_y)O_{2\pm x}$ is due to the higher elastic strain experienced by the former than latter.

It is seen from Table 8 that the O/M decreases with decrease in U content in the sample. The trend in the variation of O/M with respect to concentration of U is in agreement with the O/M measured by spectrophotometric technique (Table 8). However, the O/M ratio determined by XPS is higher than that determined by spectrophotometric technique for all the mixed oxides (Table 8). This could be due to the fact that the oxygen defect produced by the introduction of La^{3+} into U^{4+} sites is easily filled by the oxygen supplied from the atmosphere whereas in the inside of the pellet the oxygen supply may not be enough resulting in the retention of the defect. This phenomenon was also observed on the XPS studies on $(U_{1-y}Gd_y)O_{2\pm x}$ by Miyake et al. [32]. This is because the O/M ratio obtained by XPS technique is valid only few atomic layers from the surface of the sample and the same are more prone for oxidation than the bulk whereas that determined by the spectrophotometric technique is that of the bulk. In La doped UO_2, stable oxygen vacancies were created because of lower oxidation state of La^{3+} in the mixed oxides. But U^{4+} has a tendency to get to higher oxidation states and would try to accommodate the oxygen within the surface or subsurface layers to maintain charge neutrality. As a result there will be distribution of U^{5+} and U^{6+} along with usual lattice of U^{4+} and La^{3+}. In case of La rich mixed oxides, the oxides show a domination of higher oxidation states of U (+5 and +6 state) which resulted in higher O/U ratio. However, as the U contents in these mixed oxides are insufficient to compensate the oxygen vacancies created on doping with La of +3 valency, the surface O/M of these mixed oxides are less than 2. In case of U rich mixed oxides, O/M ratio is higher than 2.0 and in case of La rich oxides the ratio is lower than 2.0. Similar results were observed in our previous study [25] on $(U_{1-y}Ce_y)O_2$.

5. Conclusions

Heat capacity of $(U_{1-y}La_y)O_{2\pm x}$ ($y = 0.2$, 0.4, 0.6, and 0.8) was measured by DSC in the temperature range 298–800 K. Enthalpy

increment measurements were carried out by drop calorimetry in the temperature range 773–1800 K. Heat capacity was computed from the enthalpy increment data. Considerable anomalous increase in the heat capacity was observed for $(U_{1-y}La_y)O_{2\pm x}$ ($y = 0.4$, 0.6, and 0.8) and no such anomaly was observed for $y = 0.2$. This phenomenon is attributed to be due to the formation of Frenkel pair of defects of oxygen. The onset temperature of heat capacity anomaly did not vary with the concentration of La in the sample. The enthalpy of the formation of defect is in the range of 1.31–1.33 eV. The higher onset temperature of heat capacity anomaly of $(U_{1-y}La_y)O_{2\pm x}$ compared to that doped with $(U_{1-y}Gd_y)O_{2\pm x}$ is due to higher enthalpy of defect formation in the former than the latter. This in turn, is due to the higher elastic strain experienced by the former than latter. From the XPS analysis of the mixed oxides, it was found that the O/M ratio at the surface was found to be higher than that of the bulk and is governed by the major element in the oxide. The O/M ratios of the La rich mixed oxides are less than 2 whereas that for U rich mixed oxides are more than 2.

References

[1] E.A.C. Crouch, At. Data Nucl. Data Tables 19 (5) (1977) 501–502 (Academic Press, New York and London).
[2] R.J. Beals, J.H. Handwerk, B.J. Wrona, J. Am. Ceram. Soc. 52 (11) (1969) 578–581.
[3] K. Naito, J. Nucl. Mater. 167 (1989) 30–35.
[4] H. Inaba, K. Naito, M. Oguma, J. Nucl. Mater. 149 (1987) 341–348.
[5] T. Matsui, Y. Arita, K. Naito, J. Radioanal. Nucl. Chem. 143 (1) (1990) 149–156.
[6] T. Matsui, T. Kawase, K. Naito, J. Nucl. Mater. 186 (1992) 254–258.
[7] K.C. Mills, F.H. Ponsford, M.J. Richardson, Thermochim. Acta 139 (1989) 107–120.
[8] Y. Arita, T. Matsui, S. Hamada, Thermochim. Acta 253 (1995) 1–9.
[9] Y. Arita, H. Hamada, T. Matsui, Thermochim. Acta 247 (1994) 225–236.
[10] H. Inaba, K. Naito, M. Oguma, H. Masuda, J. Nucl. Mater. 137 (1986) 176–178.
[11] R. Venkata Krishnan, G. Panneerselvam, P. Manikandan, M.P. Antony, K. Nagarajan, J. Nucl. Radiochem. Sci. 10 (1) (2009) 19–26.
[12] M. Amaya, K. Une, K. Minato, J. Nucl. Mater. 294 (2001) 1–7.
[13] Y. Takahashi, M. Asou, J. Nucl. Mater. 201 (1993) 108–114.
[14] Y. Takahashi, M. Asou, Thermochim. Acta 223 (1993) 7–22.
[15] R.A. Verrall, P.G. Lucuta, J. Nucl. Mater. 228 (1996) 251–253.
[16] P.G. Lucuta, H. Matzke, R.A. Verrall, H.A. Tasman, J. Nucl. Mater. 188 (1992) 198–204.
[17] R. Venkata Krishnan, G. Panneerselvam, M.P. Antony, K. Nagarajan, J. Nucl. Mater. 403 (2010) 25–31.
[18] R. Venkata Krishnan, K. Nagarajan, Thermochim. Acta 440 (2006) 141–145.
[19] R. Venkata Krishnan, K. Nagarajan, P.R. Vasudeva Rao, J. Nucl. Mater. 299 (2001) 28–31.
[20] Synthetic Sapphire Al_2O_3, Certificate of Standard Reference Materials 720, National Bureau of Standards, U.S. Department of Commerce, Washington, DC 20234, USA, 1982.
[21] L.B. Pankratz, Bull. US Bur. Mines (1984).
[22] J.K. Fink, J. Nucl. Mater. 279 (2000) 1–18.
[23] R. Kandan, R. Babu, P. Manikandan, R. Venkata Krishnan, K. Nagarajan, J. Nucl. Mater. 384 (3) (2009) 231–235.
[24] S. Bera, S.K. Sali, S. Sampath, S.V. Narasimhan, V. Venugopal, J. Nucl. Mater. 255 (1998) 26–33.
[25] S. Bera, V.K. Mittal, R. Venkata Krishnan, T. Saravanan, S. Velmurugan, K. Nagarajan, S.V. Narasimhan, J. Nucl. Mater. 137 (2006) 6–10.
[26] E.S. Ilton, J.-F. Boily, P.S. Bagus, Surf. Sci. 601 (2007) 908–916.
[27] S. Mickevicius, S. Grebinskij, V. Bondarenka, B. Vengalis, K. Sliuziene, B.A. Oflowski, V. Osinniy, W. Drube, J. Alloys Compd. 423 (2006) 107–111.
[28] C. Muggelberg, M.R. Castell, G.A.D. Briggs, D.T. Goddard, Appl. Surf. Sci. 142 (1999) 124–128.
[29] D.J. Kim, J. Am. Ceram. Soc. 72 (8) (1989) 1415–1421.
[30] J.A. Kilner, R.J. Brook, Solid State Ionics 6 (3) (1982) 237–252.
[31] J.A. Kilner, in: R. Metselaar, H.J.M. Heijligers, J. Schoonman (Eds.), Proceedings of the Second European Conference, Elsevier, Amsterdam, 1983, pp. 189–192.
[32] C. Miyake, M. Kanamaru, S. Imoto, J. Nucl. Mater. 138 (1986) 36–39.